WILEY-VCH

Characterization of Nanophase Materials

Edited by Zhong Lin Wang

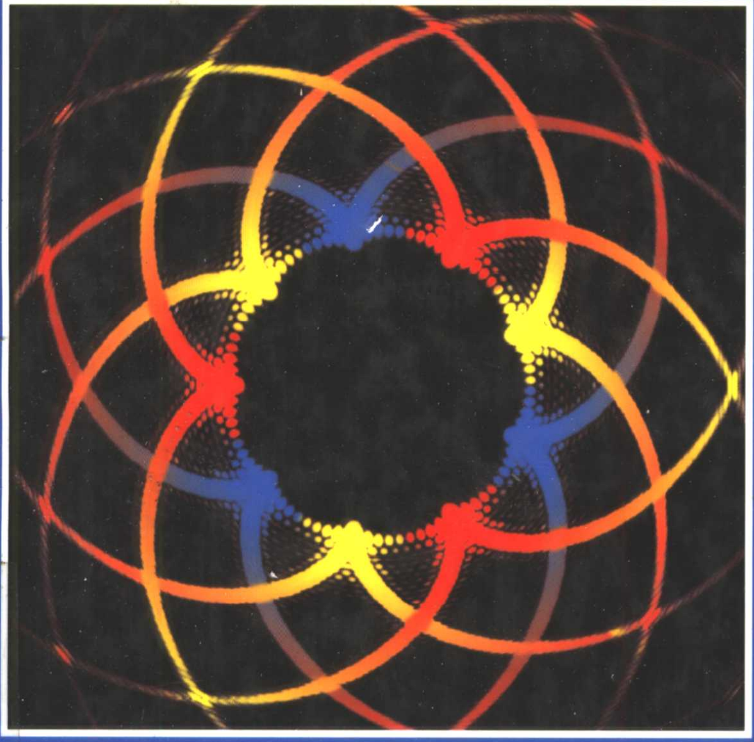

Characterization of Nanophase Materials

Edited by
Zhong Lin Wang

WILEY-VCH

Weinheim · New York · Chichester · Brisbane · Singapore · Toronto

List of Contributers

S. Amelinckx
EMAT
University of Antwerp (RUCA)
Groenenborgerlaan 171
Antwerp B-2020
Belgium

Moungi G. Bawendi
Department of Chemistry, 6-223
Massachusetts Institute of Technology
Cambridge, MA 02139
USA

C. Burda
School of Chemistry and Biochemistry
Georgia Institute of Technology
Atlanta GA 30332-0400
USA

A. Chemseddine
Physikal Chemistry Department (CK)
Hahn-Meitner-Institut
Glienicker Straße 100
14109 Berlin
Germany

Lifeng Chi
Physikalisches Institut
Westfälische Wilhelms-Universität
Münster
Wilhelm-Klemm-Straße 10
48149 Münster
Germany

Walt de Heer
School of Physics
Georgia Institute of Technology
Atlanta GA 30332-0430
USA

Mostafa A. El-Sayed
Laser Dynamics Laboratory
School of Chemistry and Biochemistry
Georgia Institute of Technology
Atlanta GA 30332-0400
USA

Stephen Empedocles
Department of Chemistry, 6-223
Massachusetts Institute of Technology
Cambridge, MA 02139
USA

Gregory J. Exarhos
Pacific Northwest National Laboratory
Battelle Blvd.
Richland, Washington 99352
USA

Travis Green
Laser Dynamics Laboratory
School of Chemistry and Biochemistry
Georgia Institute of Technology
Atlanta GA 30332-0400
USA

Blair D. Hall
Measurement Standards Laboratory
Caixa Postal 6192 – CEP 13083-970
Campinas, São Paulo
Brasil (Brazil)

C. Landes
Laser Dynamics Laboratory
School of Chemistry and Biochemistry
Georgia Institute of Technology
Atlanta GA 30332-0400
USA

S. Link
Laser Dynamics Laboratory
School of Chemistry and Biochemistry
Georgia Institute of Technology
Atlanta GA 30332-0400
USA

R. Little
Laser Dynamics Laboratory
School of Chemistry and Biochemistry
Georgia Institute of Technology
Atlanta GA 30332-0400
USA

Jingyue Liu
Monsanto Company
Analytical Sciences Center
800 N. Lindbergh Blvd., U1E
St. Louis, Missouri 63167
USA

Jun Liu
Pacific Northwest National Laboratory
Battelle Blvd.
Richland, Washington 99352
USA

Meilin Liu
School of Materials Science
and Engineering
Georgia Institute of Technology
Atlanta GA 30332-0245
USA

Robert Neuhauser
Department of Chemistry, 6-223
Massachusetts Institute of Technology
Cambridge, MA 02139
USA

Janet M. Petroski
Laser Dynamics Laboratory
School of Chemistry and Biochemistry
Georgia Institute of Technology
Atlanta GA 30332-0400
USA

Christian Röthig
Physikalisches Institut
Westfälische Wilhelms-Universität
Münster
Wilhelm-Klemm-Straße 10
48149 Münster
Germany

Zhong Shi
School of Materials Science
and Engineering
Georgia Institute of Technology
Atlanta GA 30332-0245
USA

Kentaro Shimizu
Department of Chemistry, 6-223
Massachusetts Institute of Technology
Cambridge, MA 02139
USA

Daniel Ugarte
Laboratorio Nacional de Luz Sincrontron
Caixa Postal 6192 – CEP 13083-970
Campinas, São Paulo
Brasil (Brazil)

G. Van Tendeloo
EMAT
University of Antwerp (RUCA)
Groenenborgerlaan 171
Antwerp B-2020
Belgium

Li-Qiong Wang
Pacific Northwest National Laboratory
Battelle Blvd.
Richland, Washington 99352
USA

Zhong Lin Wang
School of Materials Science
and Engineering
Georgia Institute of Technology
Atlanta GA 30332-0245
USA

Daniela Zanchet
Laboratorio Nacional de Luz Sincrontron
Caixa Postal 6192 – CEP 13083-970
Campinas, São Paulo
Brasil (Brazil)

List of Symbols and Abbreviations

a	lattice parameter
A	area of an electrode
A_d	area on the CRT display
$A(\mathbf{K})$	aperture function
$A(k)$	backscattering amplitude
A_s	area scanned on the sample
B	magnetic field
c	lattice parameter
c	spring constant of the cantilever
c	elastic constant
C_0	capacitance of the empty cell used for transfer function measurement, $C_0 = \varepsilon_0 A/d$.
$C_{1/2}$	capacities
C_{dl}	double-layer capacitance
C_f	sensitivity constant derived from the Sauerbrey relationship
c_j	concentration of species j
c_j^*	bulk concentration of species j
Cs	spherical abberation coefficient
d	distance
d	resonator thickness
d	separation between two parallel electrode in an impedance measurement
d	thickness
D	Debye-Waller factor
D_j	diffusion coefficient of species j
$D(\mathbf{K})$	transmission function of the detector
D_Q	dissipation coefficient corresponding to the energy losses during oscillation
E	photoelectron energy
E	polarization of the emitted light
E	voltage or electric potential
ΔE	Stark shift
E_0	accelerating voltage
E_o	threshold energy
$E_{1/2}$	half-wave potential (in voltammetry)
E_b	biexciton binding energy
E_i	initial potential
E_p	peak potential
ΔE_P	$\lvert E_P{}^A - E_P{}^C \rvert$ in CV
$E_{p/2}$	potential where $I = I_p/2$ in LSV or CV
F	electric field
F	faraday constant, $F = 96{,}485$ C/equiv
F	net force
Δf	lens defocus
Δf	measured frequency change

f_0	frequency of a quartz resonator prior to a mass change
$F'(d)$	force gradient
$F(\bar{k})$.	structure amplitude
$f(s)$	scattering factor
$\mathrm{FT}[V_p(\mathbf{b})]$	Fourier transform of the crystal potential
Fz	attractive force
G	reciprocal lattice vector
h	piezoelectric stress constant
H	total Hamiltonian
I	transmitted intensity
I	tunneling current
I_o	incident beam intensity
$I_0(\mathbf{x})$	intensity distribution of the incident probe
$I_0(\Delta)$	integrated intensity of the low-loss region including the zero-loss peak for an energy window Δ
i_f	faraday current
$I_N(s)$	power scattered per unit solid angle in the direction defined by s
I_p	peak current
i_r	current during reversal step
I_{SE}	total integrated SE intensity
$I(\mathbf{X})$	image intensity
j	coordination shell index
j	imaginary unit, $j = (-1)^{1/2}$
J	net electronic angular momentum
J_0	exchange current density
J_{ij}	exchange energy constants
Jn	Bessel functions of order n.
k	electron wave-vector
k	spring constant
K	anisotropy energy
$\bar{K}$	wavevector of the scattered wave
K_0	cut-off wave-vector
$\bar{K}_o$	wavevector of the incident wave
k^o	standard heterogeneous rate constant
k_F	Fermi wave vector
l	length
L	average escape-depth
L	total orbital angular momentum
L_d	thickness of a Nernst diffusion layer
m	electron mass
M	magnetization
M	magnification
Δm	mass change
$M_r(\omega)$	modulus function, $M_r(\omega) = [\varepsilon_r(\omega)]^{-1}$
MW	apparent molar mass (g mol^{-1})
$M_{\mu\nu}$	tunneling matrix element
n	density
n	number of electrons involved in an electrochemical process
N	number of identical atoms in the same coordination shell
p	momentum

$P(\mathbf{b},\Delta z)$	propagation function
$P_{l,m}$	associated Legendre function
P_j	depolarization factors for the three axes A, B, C of the nanorod with A > B = C
Q	charge
$Q(\mathbf{b},z+\Delta z)$	phase grating function of the slice
Q_{dl}	charge due to double layer charging
$Q(\mathbf{K})$	Fourier transform of the object transmission function
$q(\mathbf{x})$	transmission function of the object
r	distance between absorbing and neighbor atoms
R	gas constant
R	radius
R	resistance
R_b	bulk resistance of a electrolyte
R_{ct}	resistance to charge transfer at electrolyte-electrode interfaces
r_{m}	radius
r_{mn}	distance between atom *m* and atom *n*
R_{mt}	steady state mass-transfer resistance
$\mathbf{S}$	total spin angular momentum
$S_o^2(k)$	amplitude reduction factor due to many-body effects
$\mathbf{S}_{\mathrm{i}}$	spin operator of i^{th} electron
t	time
T	absolute temperature
T	material thickness
T_1	energy relaxation
T_2	dephasing time
T_{c}	Curie temperature
$T(\mathbf{K})$	transfer function of the microscope
$t_{\mathrm{obj}}(x,y)$	inverse Fourier transform of $T(\mathbf{K})$
$t(\mathbf{x})$	amplitude distribution of the incident probe
$\mathbf{u}$	reciprocal space vector
U	tunneling voltage
U_0	acceleration voltage
v	linear potential scan rate
v	electron velocity
V	volume
V_m	molar volume
$V\mathrm{p}(\mathbf{b})$	hickness-projected potential of the crystal
W	distance between tip and sample
$\mathbf{X}$	beam position
Δx	rms atomic displacement
x_0	impact parameter
$Y(\omega)$	$Y(\omega)=[Z(\omega)]^{-1}$, admittance function
Δz	displacement of the cantilever and piezo
z_i	charge carried by species i signed units of electronic charge
Z_{w}	Warburg impedance
$Z(\omega)$	impedance function
α, β	angle
α, β	parameters
$\alpha_{\mathrm{a}}, \alpha_{\mathrm{c}}$	anodic and cathodic charge transfer coefficient

β	asymmetry parameter for a one-electron process
$\chi(k)$	EXAFS oscillations
$\chi(\mathbf{K})$	aberration function of the objective lens
$\chi(T)$	magnetic susceptibility
$\chi(\sigma t)$	tabulated number
Δ	defocus value
δ	temporal phase angle between the charging current and the total current
ε_0	absolute permettivity (or the permittivity of free space)
ε_m	dielectric constant
ε_Q	dielectric constant of quartz
ε_r	relative permittivity of a material
ε_r'	dielectric constant
$\varepsilon(\omega)$	dielectric function
ϕ	tilt angle between μ and sample plane
ϕ	total photoelectron phase shift
Φ	workfunction
$\phi(k)$	total phase shift
$\phi(r)$	electronic ground state wave function
$\phi(\mathbf{x})$	projected specimen potential along the incident beam direction
λ	wavelength
$\lambda(k)$	photoelectron mean free path
μ	absorption coefficient
μ	paramagnetic atom
μ	transition dipole vector
μ_o	atomic absorption coefficient
μ_B	Bohr magneton
$\mu(E)$	absorption coefficient associated with a particular edge
$\Delta\mu(E)$	change in the atomic absorption across the edge
$\mu_o(E)$	absorption coefficient of an isolated gold atom
$\mu_{Exc.}$	exciton dipole moment
μ_Q	shear modulus of AT-cut quartz
μ_S	net surface dipole moment
v_{tr}	transverse velocity of sound in AT-cut quartz (3.34×10^4 m s^{-1})
θ	angle between emission polarization and projection of μ onto the sample plane
θ	scattering angle
θ	temporal phase angle
θ_B	Bragg diffraction angle
ρ_Q	density of quartz
ρ_S	density of states of sample
$\rho_S(z,E)$	local density of states of the sample
ρ_T	density of states of tip
σ	atomic scattering cross-section
σ	interaction constant
σ	total Debye-Waller factor (including static and dynamic contributions)
$\sigma_{i,el}$	ionic conductivity (Ω^{-1}cm^{-1}) of an electrolyte
$\sigma A(\Delta,\beta)$	energy and angular integrated ionization cross-section
σ_{ext}	total extinction coefficient
τ	forward step duration time in a double-step experiment

τ	relaxation time
ω	angular frequency
Ω	atomic volume
Ψ	total electronic wave function
$\Psi(\mathbf{K})$	exit wave function
$\Psi(\mathbf{K}, \mathbf{X})$	amplitude function
$\psi(\mathbf{u})$	Fourier transform of the wave
$\Psi(x, y)$	transmitted wave function
ADF	annular dark-field
AE	Auger electron
AFM	atomic force microscopy
bcc	body-centered cubic
BF	bright-field
CA	chronoamperometry
CB	conduction band
CBED	convergent beam electron-diffraction
CCD	charge coupled device
CCM	constant current mode
CE	counter electrode
CEND	coherent electron nanodiffraction
CHA	concentric hemispherical analyzer
CHM	constant height mode
CID	chemical interface damping
C.L	cathodoluminescence
CMA	cylindrical mirror analyzer
CP	cross-polarization
CPR	current pulse relaxation
CRT	cathode-ray-tube
CTAB	cetyltrimethylammonium bromide
CTAC	cetyltrimethylammonium chloride
CTF	contrast transfer function
CV	cyclic voltammetry
DAS	dynamic-angle spinning
dec	decahedron
DiI	1,1′-dioctadecyl-3,3,3′,3′-tetramethylindocarbocyanine
DFA	Debye function analysis
DOR	double-rotation
DSTEM	dedicated scanning transmission electron microscopy
EDS	energy dispersive x-ray spectroscopy
EELS	energy-loss spectroscopy
EFM	electric force microscopy
EF-TEM	energy-filtered transmission electron microscopy
ELD	electroless deposition
ELNES	energy-loss near edge structure
EQCM	electrochemical quartz crystal microbalance
EXAFS	extended x-ray absorption fine structure
fcc	face-centered-cubic
FEG	field-emission gun
FE-SAM	field emission scanning Auger microscope

FE-TEM	field-emission transmission electron microscopy
FFM	frictional force microscopy
FLDOS	local density of states near the Fermi energy
FM	frequency modulation
FMM	force modulation microscopy
FWHM	full-width-at-half-maximum
GITT	galvanostatic intermittent titration technique
GMR	giant magnetoresistance
HAADF	high-angle annular dark-field
HOMO	highest occupied molecular orbital
HOPG	highly oriented pyrolytic graphite
HRTEM	high resolution transmission electron microscopy
ico	icosahedron
IR	infrared spectroscopy
IS	impedance spectroscopy
LABF	large angle bright-field
LB	Langmuir-Blodgett
LNLS	Brazilian National Synchrotron Laboratory
LO	longitudinal-optical
LSV	linear sweep voltammetry
LTS	local tunneling spectroscopy
LT-STM	low-temperature scanning tunneling microscopy
LUMO	lowest unoccupied molecular orbital
MAS	magic angle spinning
MECS	multiple expansion cluster source
MFM	magnetic force microscopy
MIDAS	microscope for imaging, diffraction, and analysis of surfaces
MIEC	mixed ionic-electronic conductor
MTP	multiply-twinned particles
NCA	nanocrystal arrays
NCS	nanocrystal superlattices
NMR	nuclear magnetic resonance
NQ	napthoquinone
NSOM	near-field scanning optical microscopy
OCV	open-circuit voltage
OD	optical density
ODPA	octadecylphosphonate
PCTF	phase-contrast transfer function
PEELS	parallel electron energy-loss spectroscopy
PL	photoluminescence
POA	phase object approximation
PS	polystyrene
PSD	position-sensitive detector
PSP	poly(styrenephosphonate diethyl ester)
PVK	polyvinylcarbazole
P″VP	poly(2-vinylpyridine)
QCM	quartz crystal microbalance
QCNB	quartz crystal nanobalance
QDQW	quantum-dot quantum-well
QDs	quantum dots

RE	reference electrode
REDOR	rotational-echo double resonance
ROMP	ring-opening metathesis polymerization
SA	self-assembly
SAM	scanning Auger microscopy
SAMs	self-assembled monolayers
SAXS	small-angle elastic x-ray scattering
SCAM	scanning capacitance microscopy
SE	secondary electron
SEMPA	scanning electron microscopy with polarization analysis
SEDOR	spin-echo double resonance
SES	lower case Secondary electron spectroscopy
SET	single-electron-tunneling
SFM	scanning force microscopy
SNOM	scanning near-field optical microscopy
SP	single-pulse
SPM	scanning probe microscopes
SPs	surface plasmons
STEM	scanning transmission electron microscopy
STM	scanning tunneling microscopy
STS	scanning tunneling spectroscopy
T3	2,5‴-bis(acetylthio)-5,2′,5′,2″-terthienyl
TAD	thin annular detector
TADBF	thin annular detector for bright-field
TADDF	thin annular detector for dark-field
TEM	transmission electron microscopy
TDS	thermal diffuse scattering
TO	truncated octahedral
TP	thiophenol
UHV	ultrahigh vacuum
VB	valence band
VOA	virtual objective aperture
WE	working electrode
WPOA	weak scattering object approximation
XANES	x-ray absorption near edge structure
XAS	x-ray absorption spectroscopy
XEDS	x-ray energy-dispersive spectroscopy
XPS	x-ray photoelectron spectroscopy
XRD	x-ray diffraction

Contents

4 Scanning Transmission Electron Microscopy of Nanoparticles

Jingyue Liu

5 Scanning Probe Microscopy of Nanoclusters

Lifeng Chi and Christian Röthig

6 Electrical and Electrochemical Analysis of Nanophase Materials

Zhong Shi and Meilin Liu

7 Optical Spectroscopy of Nanophase Materials

C. Burda, T. Green, C. Landes, S. Link, R. Little, J. Petroski, M. A. El-Sayed

8 Nuclear Magnetic Resonance – Characterization of Self-Assembled Nanostructural Materials

Li-Qiong Wang, Gregory J. Exarhos, and Jun Liu

9 Photoluminescence from Single Semiconductor Nanostructures

Stephen Empedocles, Robert Neuhauser, Kentaro Shimizu and Moungi Bawendi

10 Nanomagnetism

Wal A. de Heer

11 Metal-oxide and -sulfide Nanocrystals and Nanostructures

A. Chemseddine

12 Electron Microscopy of Fullerenes and Related Materials

G. Van Tendeloo and S. Amelinckx

1 Nanomaterials for Nanoscience and Nanotechnology

Zhong Lin Wang

Technology in the twenty first century requires the miniaturization of devices into nanometer sizes while their ultimate performance is dramatically enhanced. This raises many issues regarding to new materials for achieving specific functionality and selectivity. Nanophase and nanostructured materials, a new branch of materials research, are attracting a great deal of attention because of their potential applications in areas such as electronics [1], optics [2], catalysis [3], ceramics [4], magnetic data storage [5, 6], and nanocomposites. The unique properties and the improved performances of nanomaterials are determined by their sizes, surface structures and interparticle interactions. The role played by particle size is comparable, in some cases, to the particle chemical composition, adding another flexible parameter for designing and controlling their behavior. To fully understand the impacts of nanomaterials in nanoscience and nanotechnology and answer the question of why nanomaterials is so special, this chapter reviews some of the unique properties of nanomaterials, aiming at elucidating their distinct characteristics.

1.1 Why nanomaterials?

Nanomaterials are classified into nanostructured materials and nanophase/nanoparticle materials. The former refer to condensed bulk materials that are made of grains with grain sizes in the nanometer size range, while the latter are usually the dispersive nanoparticles. The nanometer size here covers a wide range which can be as large as 100–200 nm. To distinguish nanomaterials from bulk, it is vitally important to demonstrate the unique properties of nanomaterials and their prospective impacts in science and technology.

1.1.1 Transition from fundamental elements to solid states

Nanomaterials are a bridge that links single elements with single crystalline bulk structures. Quantum mechanics has successfully described the electronic structures of single elements and single crystalline bulks. The well established bonding, such as ionic, covalent, metallic and secondary, are the basis of solid state structure. The theory for transition in energy levels from discrete for fundamental elements to continuous bands for bulk is the basis of many electronic properties. This is an outstanding question in basic science. Thus, a thorough understanding on the structure of nanocrystals can provide deep insight in the structural evolution from single atoms to crystalline solids.

Nucleation and growth are two important processes in synthesizing thin solid films. Nucleation is a process in which an aggregation of atoms is formed, and is the first step of phase transformation. The growth of nuclei results in the formation of large crystalline particles. Therefore, study of nanocrystals and its size-dependent structures and properties is a key in understanding the nucleation and growth of crystals.

1.1.2 Quantum confinement

A specific parameter introduced by nanomaterials is the surface/interface-to-volume ratio. A high percentage of surface atoms introduces many size-dependent phenomena. The finite size of the particle confines the spatial distribution of the electrons, leading to the quantized energy levels due to size effect. This quantum confinement has applications in semiconductors, optoelectronics and non-linear optics. Nanocrystals provide an ideal system for understanding quantum effects in a nanostructured system, which could lead to major discoveries in solid state physics.

The spherical-like shape of nanocrystals produces surface stress (positive or negative), resulting in lattice relaxation (expansion or contraction) and change in lattice constant [7]. It is known that the electron energy band structure and bandgap are sensitive to lattice constant. The lattice relaxation introduced by nanocrystal size could affect its electronic properties.

1.1.3 Size and shape dependent catalytic properties

The most important application of nanocrystals has been in catalysis. A larger percentage of surface atoms greatly increases surface activities. The unique surface structure, electronic states and largely exposed surface area are required for stimulating and promoting chemical reactions. The size-dependent catalytic properties of nanocrystals have been widely studied, while investigations on the shape (facet)-dependent catalytic behavior are cumbersome. The recent success in synthesizing shape-controlled nanocrystals, such as the ones dominated by {100}, {111} [8] and even {110} facets [9], is a step forward in this field.

1.1.4 Novel mechanical properties

It is known that mechanical properties of a solid depend strongly on the density of dislocations, interface-to-volume ratio and grain size. An enhancement in damping capacity of a nanostructured solid may be associated with grain-boundary sliding [10] or with energy dissipation mechanism localized at interfaces [11] A decrease in grain size significantly affects the yield strength and hardness [12]. The grain boundary structure, boundary angle, boundary sliding and movement of dislocations are important factors that determine the mechanical properties of the nanostructured materials. One of the most important applications of nanostructured materials is in superplasticity, the capability of a polycrystalline material to undergo extensive tensible deformation without necking or fracture. Grain boundary diffusion and sliding are the two key requirements for superplasticity.